Light-sheet microscopy of network activity in 3D neuronal systems

PAULINA M. WYSMOLEK[1], FILIPPO D. KIESSLER[2], KATJA A. SALBAUM[2,3], ELIJAH R. SHELTON[2], SELINA SONNTAG[2], AND FRIEDHELM SERWANE[*2,3,4]

[1]*Max Planck Institute for Medical Research, Heidelberg, Germany*
[2]*Faculty of Physics and Center for NanoScience, Ludwig-Maximilians-Universität München, Munich, Germany*
[3]*Graduate School of Systemic Neuroscience (GSN), Munich, Germany*
[4]*Munich Cluster for Systems Neurology (SyNergy), Germany*
**f.serwane@lmu.de*

Abstract: *In vitro* systems mimicking brain regions, such as brain organoids, are revolutionizing the field of neuroscience. However, characterization of their electrical activity has remained a challenge as this requires electrophysiological readout at millisecond timescale in 3D at single-neuron resolution. While custom-built microscopes used with genetically encoded sensors start to grant this access, a thorough 3D characterization of organoid neural activity has not been performed yet, limited by the combined complexity of the optical and the biological system. Here, we introduce a simple microscope for volumetric characterization of network activity with single-neuron resolution. To provide a versatile, accessible platform to the neuroscience community, we designed a minimalistic light-sheet microscope tailored to computational neuroscience tools to extract calcium traces. As a proof of principle, we created a 3D connectivity map of the neuronal network by imaging its spontaneous activity. High performance, low complexity setups such as ours will empower researchers to study the formation of neuronal networks *in vitro* for fundamental and neurodegeneration research.

Introduction

Electrophysiological readouts at single-neuron resolution are one building block to understanding of the brain. A major hurdle, however, is the limited experimental access to living human brain tissue granted by state-of-the-art recording technologies. In recent years, tremendous progress has been made with the introduction of cerebral organoids, multicellular systems derived from embryonic and induced pluripotent stem cells [2-5]. These *in vitro* models recapitulate aspects of *in vivo* neuron behaviour and tissue architecture. To what extent they replicate network function as seen *in vivo* is an open question [3, 6]. As the first functional studies of 3D neuronal network emerge[6], the experimental challenges remain strict: Neurons generate and propagate electrical signals at a millisecond timescale via action potentials. Thus, the functionality of a neuronal tissue needs to be assessed at this timescale in 3D, all at a single-neuron resolution.

Patch clamps record electrophysiological signals of single neurons within neurospheres [7, 8], cerebral organoids [9-12] and retinal organoids [13-15] with high temporal resolution (sub-milliseconds). This enables the sampling of individual action

potentials and thus the determination of inhibitory and excitatory neuronal response upon external stimulation. However, only a few individual neurons can be inspected at once which prevents the mapping of larger networks, a signature of the brain.

CMOS-based multi-electrode arrays (MEA) capture extracellular potentials created by neuronal populations which can be used to analyze 2D connectivity and neural circuits in neurospheres,[16] as well as in brain and retinal organoids [5, 17-24]. Recently, initial 3D characterization of network behavior in brain organoids was performed by combining MEA with CMOS based shank probes [6]. While electrode approaches offer unprecedented time resolution, their resolution in 3D remains limited due to the ability to place electrodes at different heights. As a result, spatial sampling in the third (z) dimension is difficult to obtain. In addition, information which neuron types build up the network is hidden due to a lack of imaging access. This is a particular drawback for characterizing organoids consisting of different neuron types, for example cerebral and retina organoids. In those systems, it is hypothesized that neuron circuits play the same crucial role for signal processing as in their *in vivo* counterparts [3, 25, 26].

Calcium imaging using fluorescence-based microscopy allows monitoring 3D network activity with simultaneous access to cell morphology[27]. The functionality of both cerebral and retinal organoids has been characterized with one- and two-photon confocal microscopy [2, 28-30]. However, experiments were performed in 2D, limited by the scanning speed of the confocal microscope. To overcome this challenge, custom light-sheet and light-field microscopes have been developed (Suppl. Table 1). Using sophisticated custom-built optical setups, functional 4D activity mapping in *Caenorhabditis elegans*, zebrafish, and primary neuron cultures have been performed at scanning rates between 0.8 to 50 Hz [31-38]. Moreover, artificial intelligence–enhanced microscopy has improved the performance of a light-field microscope in functional imaging of neuronal activity of the zebrafish brain [39]. While these setups are in principle suited to perform volumetric imaging of neuronal networks, they require advanced optical expertise in their assembly and alignment [39-49]. So far, few of these systems have been employed to study brain and retinal organoids [6]. While functional characterization of organoid network activity could be feasible via resource-intensive collaborations, a simple microscope setup would make neuronal characterization accessible to interdisciplinary research laboratories.

Here, we lower the hurdle for volumetric functional imaging by introducing a minimalistic custom-built light-sheet microscope tailored to state-of-the-art computational neuroscience tools [1]. Our setup allows for calcium imaging of a broad range of samples in physiological conditions with subcellular resolution. At the same time, it operates in the same temporal regime as complex custom-built microscopes. Our setup is tailored to widely used calcium-imaging probes, but displays orders of magnitude lower complexity and costs compared to previous implementations (Suppl. Table 1). As a proof of principle, we used our platform to record 3D neuronal network activity and created a global connectivity map of the network within three-dimensional neuron cultures. While our results constitute the first step in the activity mapping of 3D neural cultures, the platform is versatile and can be used with a range of samples from neuro-spheres to mature organoids.

Experimental setup and analysis pipeline

High speed light-sheet illumination integrated into widely-used off the shelf microscopes and control software would serve a broad community of researchers. We implemented a plug and play light-sheet module as an add-on to a standard inverted microscope where it simply replaces the microscope condenser (Fig. 1). To reduce complexity of the optics to a minimum, a static planar light-sheet configuration generated by a cylindrical lens and an aspheric lens was chosen and mounted via machined opto-mechanics components. For a flexible choice of fluorescent reporters and alignment-free light delivery, a commercial laser combiner was used. The setup contains three fiber-coupled laser lines at 488 nm, 561 nm and 643 nm. Light intensity was set via the laser combiner's analogue inputs using an Arduino controlled via Micromanager.

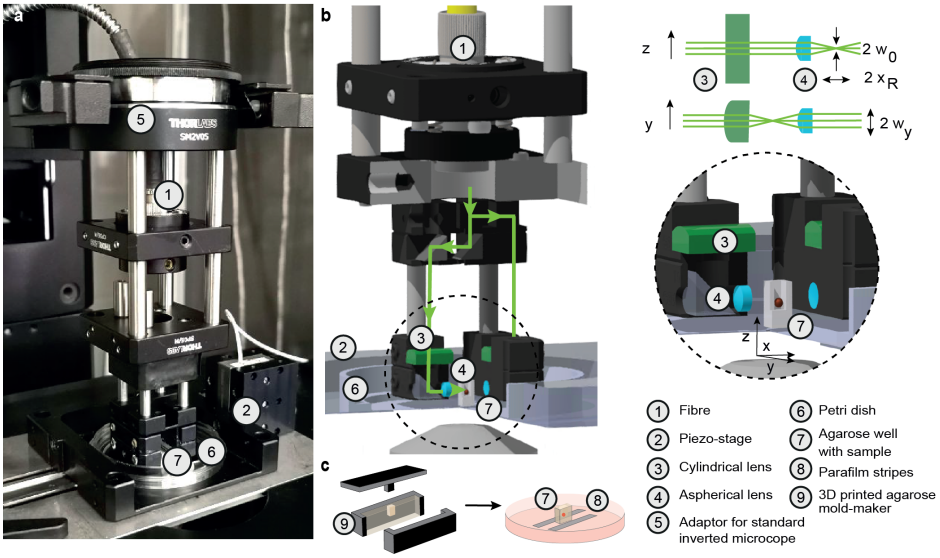

Figure 1: A minimal complexity light-sheet microscope for fast volumetric imaging *(**a**) **The light-sheet module.** Designed as an add-on to a standard inverted microscope it replaces the microscope's condenser. Volumetric imaging is achieved by movement of the sample along the optical axis using a custom piezo-stage (10 ms per frame or 5 volumes/s). (**b**) **Light-sheet optical path.** The optical beam, delivered via a fiber, is split via a cube beam splitter and directed to the sample by right-angle prisms. A static planar light-sheet is created by focusing the beam via a cylindrical lens at the back focal plane of an aspherical lens. (**c**) **Simple sample mounting.** A transparent imaging chamber is created using a 3D printed mold-maker. Liquid agarose is filled between two side plates, sealed from top with a comb. Upon gelation, the plates are removed, the well is cut-out from the gel block and placed inside a standard glass bottom Petri dish to be filled with culture medium.*

Flexible sample mounting. To allow mounting of a variety of samples and placing the light-sheet module in their close proximity, we used 50mm glass bottom dishes (Willco Wells, HBST-5040). We minimized sample movements by embedding it in an agarose well (Fig. 1c). We achieved deep imaging with long working distance water dipping objectives (20x: Olympus UMPLFLN20XW; 40x: UMPLFLN40XW). Physiological conditions (37°C, 5% CO_2) were maintained by enclosing the microscope with a custom-built incubation chamber made out of Plexi glass.

Acquisition speed tailored for Ca-imaging. To resolve responses of typical genetically encoded calcium indicators (GECIs), tens- or hundreds millisecond temporal resolution per volume is needed [50]. To acquire volumetric scans the sample is moved through the light-sheet step-wise via a custom piezo-stage. We maximized the volumetric scanning rate by minimizing the load on the stage and inverting the direction of movement after each z-stack completion. As a result, the setup allowed for volumetric scanning at 10 ms/plane, limited by the rate of camera acquisition (100 fps).

Subcellular optical resolution. To determine the microscope's resolution, we characterized the light-sheet parameters and the system's point spread function (PSF) (Fig. 2). The lateral resolution mainly depends on the numerical aperture of the objective. The axial resolution is predominantly influenced by the thickness of the anisotropic Gaussian beam light-sheet. It is parametrized by its beam waist w_0 which determines its thickness as $2w_0$ and its Rayleigh length $x_R = n\,\pi\,{w_0}^2/\lambda$ with wavelength λ and refractive index n. Its lateral extension is given by its $1/e^2$ width w_y. To quantify those parameters, we imaged the light-sheet's transversal illumination

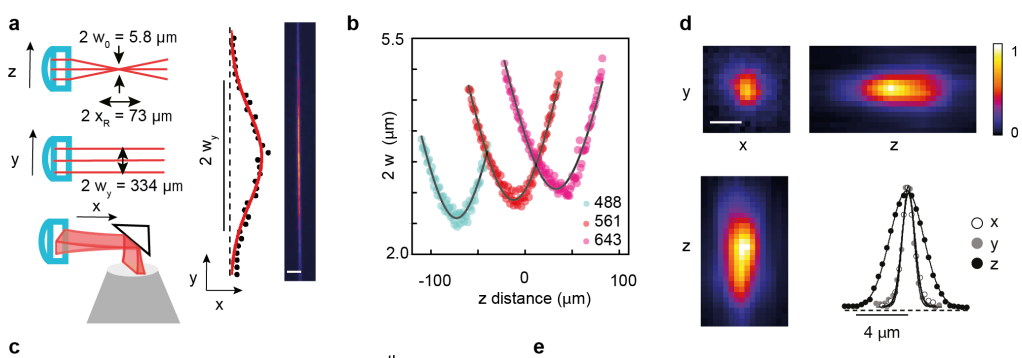

c

λ [nm]	exp 2 w_0 (µm)	exp 2 x_R (µm)	theo 2 w_0 (µm)	theo 2 x_R (µm)
488	5.2 ± 0.1	65 ± 1	3.5	44
561	5.8 ± 0.1	73 ± 1	4.0	59
643	6.1 ± 0.1	81 ± 1	4.6	77

e

Obj. / σ_{561nm}	lateral (µm) σ_x	lateral (µm) σ_y	axial (µm) σ_z	theo (µm) σ_{xy}	theo (µm) σ_z
20x/ 0.5 W	0.8 ± 0.2	1.0 ± 0.2	1.7 ± 0.2	0.7	2.0
40x/ 0.8 W	0.5 ± 0.1	0.4 ± 0.1	1.1 ± 0.3	0.4	1.5

Figure 2: Light-sheet microscopy with sub-cellular resolution. (a-c) Characterization of the light-sheet parameters. *(**a**) The light-sheet propagates along the x-axis as an elliptical Gaussian beam characterized by its thickness $2\,w_0$, its Rayleigh length x_R and its width $2\,w_y$. The parameters were determined by imaging the transversal illumination profiles. (**b**). Parameters w_0 and x_R are quantified by fitting a hyperbolic function (black line) to the measurements w(z). The light-sheet thickness remains well below 10 microns, allowing optical sectioning of the sample. Multicolour imaging is possible as the Rayleigh length is comparable to the chromatic shift (**c**). (**d-e**) **Quantification of the 3D resolution.** The PSF was measured by imaging gel-embedded fluorescent beads. (**e**) Values displayed in the table are mean $1/e$ widths ($\sigma_{x,y,z}$) for profiles along the three axes with standard deviation measured for multiple beads for two objective lenses using the 561 nm laser. Scale bars: 25 µm (**a**), 1 µm (**d**). n=6 in (20x; **c,e**); 12 in (40x,xy; **e**), n=7 (40x,z;**e**).*

profile by deflecting the light into the detection path using a $45°$ tilted mirror. Different planes along the propagation axis x were imaged by translating the mirror with respect to the light-sheet and the objective. Each image was fitted with a 2D Gaussian and $w(x)$ and $w_y(x)$ was extracted. Fitting $w(x)$ yields the light-sheet's waist w_0 and its Rayleigh length x_R (Fig. 2a-c). The characterization was performed for all three laser

lines. The thickness of the light-sheet remains well below 10 microns and thus is comparable to typical light-sheet setups (Suppl. Table 1). The recorded chromatic focus shift is on the same order of magnitude as the Rayleigh length of the light-sheet beam, allowing simultaneous multicolor imaging (Fig 2b). To measure the 3D resolution, we recorded the PSF by imaging gel-embedded 170 nm fluorescent beads (Fig. 2d). For each bead, we measured the lateral and the axial intensity profiles along two perpendicular axes in three central planes (xy, xz, yz) and fitted a Gaussian function. The $1/e$ width $\sigma_{x,y,z}$ was taken as the resolution measure. With both objectives, single-neuron resolution in all 3 dimensions is obtained in agreement with the theoretical prediction (Fig. 2e).

Culture of 3D neuronal networks. 3D neuron cultures were grown according to retina organoid protocols [51] using mouse embryonic stem cells (mESCs) (Materials and Methods). To record Calcium activity, a mESC line endogenously expressing a red fluorescence calcium sensor (R-GECO1.0) [62] (Fig. 3, Suppl. Fig. S2) was used. To allow imaging of the positions of individual cells, the cell line constitutively expressed a nuclear marker, a *H2B-GFP* fusion protein. First, embryoid bodies were formed via the aggregation of a pre-defined initial number of mECs cells in U-bottom well plates (3000 cells per well). Neural differentiation was triggered and proceeded for the next 7 days via the addition of Matrigel and differentiation medium under physiological conditions (5% CO2, 37°C). To optimize differentiation into specific neuron subtypes, the sample was then transferred to 40% O2, 5% CO2 and 37°C [61]. While the maximum sample growth time was limited to two weeks (see Materials and Methods), imaging and characterization was performed on day 12. The neural identity of the 3D culture could be confirmed via immunofluorescence staining (Fig. 3, Suppl. Fig. S2).

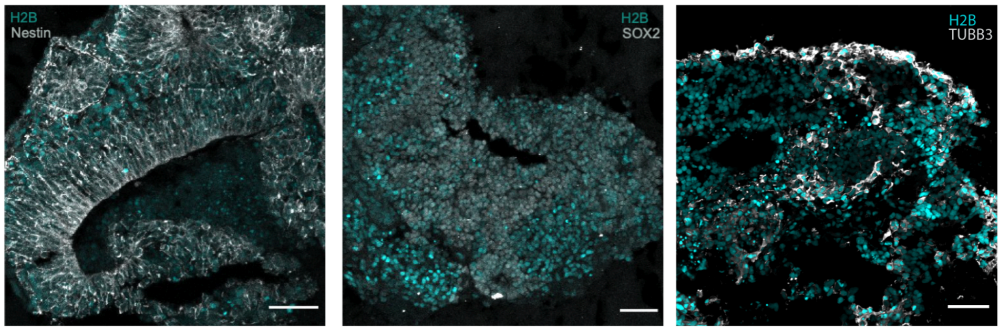

Figure 3: Confocal microscopy images of cryo-sections of the 3D neuron culture*. The presence of Nestin (A) and SOX2 (B) within rosette-like structures are signatures for neural progenitors (SOX2) and neuroepithelial cells (Nestin), respectively[52-55]. Both cell-specific markers are present in neurosphere cultures [56, 57] as well as retinal neurospheres [58]. Class 3 ß-tubulin (TUBB3) binds microtubules in neurons and is also present in neurospheres [57, 59]. Scale bar: 50 µm.*

Optimized imaging parameters. To image neurons with sufficient resolution in the z direction, planes were spaced at less than half a neuron diameter, $\Delta z = 3\,\mu m$. Furthermore, the volumetric acquisition speed was matched the typical decay time of

fluorescent Ca sensors. The R-GECO sensor has a 0.09 ± 0.02 s time-to-half-rise and 0.78 ± 0.13 s time-to-half-decay of action potential-evoked fluorescence [60]. As higher temporal resolution increases the performance of the algorithm we oversampled the decay time by a factor of 4. The scanning time in our setup can be increased for brighter indicators with faster dynamics. To reduce the size of acquired data while preserving sufficient spatial resolution, we performed 4x4 binning in xy to obtain recording volumes with 512 x 512 x 30 voxel, leading to a voxel size of (1.3x1.3x3) μm^3 for the 20x objective and (0.65x0.65x3) μm^3 for the 40x objective. With these settings, we achieve a volumetric rate of 5 Hz within an observation volume of (666x666x60) μm^3 and (333x333x60) μm^3, respectively, which is comparable to state-of-the-art setups (Suppl. Table 1).

Neuron trace extraction. Extracting the activity of densely packed neurons requires (i) the separation of spatially overlapping neurons and (ii) their discrimination from the background signal containing non-firing neurons. While several analysis packages are available (SIMA[61], CNMF-E [62], Suite2p [63], ABLE [64], SCALPEL [65], MIN1PIPE [66], SamuROI [67]), we chose CaImAn[1] because of its ability to operate on 3D data [1]. First, motion correction is performed via image registration. Next, the detection of regions of interest (ROI) is carried out followed by the extraction of the temporal fluorescence signal and static neuron segmentation using a constrained non-negative matrix factorization (CNMF) [68]. To distinguish active neurons from the fluorescent background, the 4D recordings are separated into three main contributions: the spatiotemporal Ca2+ activity AC, a background term B accounting for long term drifts and out of focus fluorescence and a noise term E. In a final step, the reconstructed signal Y is obtained as an outer product of the spatial matrix A and temporal matrix C as

$$Y = AC + B + E$$

CaImAn performs best for two-photon microscopy data due to the reduced background B and noise term E compared to data acquired with single-photon microscopes. Therefore, we introduced crucial pre- and postprocessing steps as highlighted in Fig. 4 to remove large-scale fluorescence background not caused by Ca-fluctuations. First, to correct for sample bleaching, we normalized the pixel intensities of each frame by

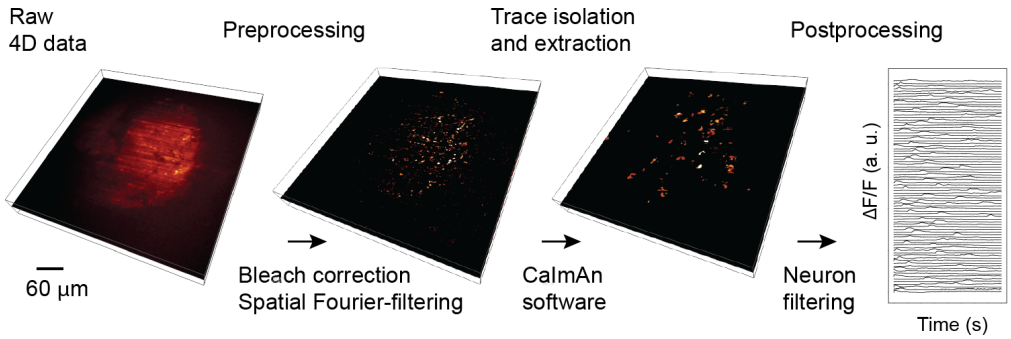

Figure 4: Processing pipeline to extract neuronal signals. *To remove the fluorescent background in a first step, the sample is bleach-corrected and spatially filtered via a Fourier filter. Neuronal traces are extracted in 3D using CaImAn [1]. In a final step, neurons are size filtered and the temporal traces are filtered according to their variance (see Materials and Methods).*

their median. After this, two light-sheet-typical artifacts remained [71]: horizontal stripes arising from the shade of optically dense objects and out-of-focus fluorescence due to the finite thickness of the light-sheet. As a discriminator for filtering we used the difference in spatial footprint of (almost point-like) neurons and the global large-scale background. To this end, a spatial Fourier-transformation was computed for each 2D image. A spatial delta-function (neuron) is widely distributed in Fourier space. In contrast, the large-scale fluorescence background and the stripe artifacts are concentrated to distinct regions corresponding to low spatial frequencies. To mask those Fourier regions for filtering, the temporal variance of each pixel in Fourier space was taken (Materials and Methods). After this preprocessing, CaImAn's motion correction algorithm was applied before temporal volumetric segmentation. In the final post-processing step, we applied a volume threshold $(710\ \mu m^3 < \mathrm{V} < 7605\ \mu m^3)$, based on typical neuron morphology. To eliminate false positive neurons caused from drifts in the residual background, the traces were filtered according to their variance. Traces that do not match either of the criteria were excluded from further analysis. In a final step, the remaining traces were normalized by a linear transformation to the [0,1] interval via $\Delta F/F = (F - F_{min})/(F_{max} - F_{min})$.

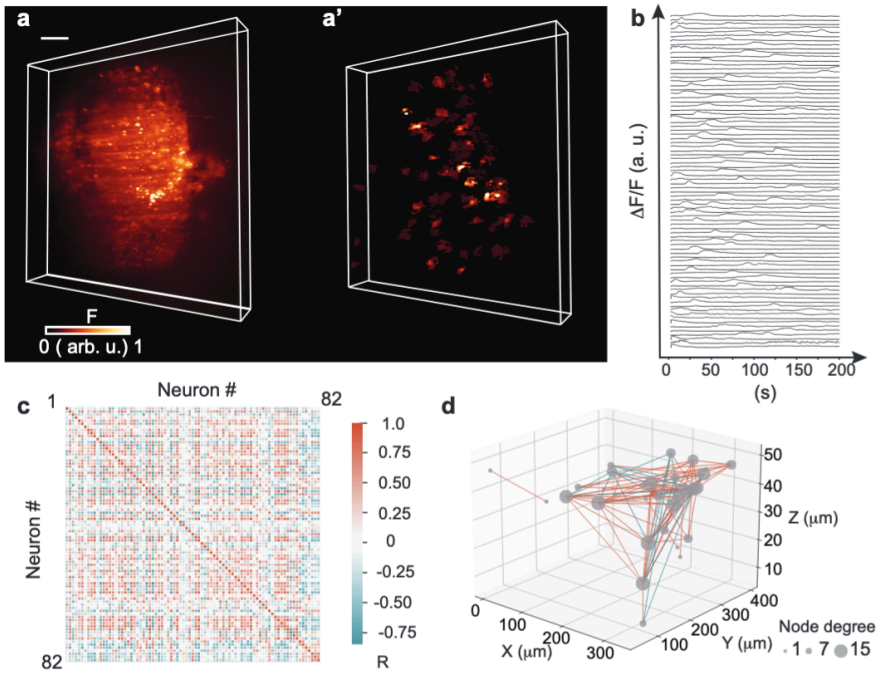

Figure 5: Quantification of neuronal responses in 3D neuron cultures. *(**a**) 3D lightsheet image of a single timepoint (R-GECO1.0 calcium sensor, raw data). (**a'**) Same image after the processing pipeline. Only active neurons remain in the observation volume. (**b**) Individually normalized calcium traces. The vertical offset serves display purposes. (**c**) A Spearman rank correlation matrix between any pair of active neurons was constructed using the raw fluorescence traces, ordered according to their distance from the centre of mass (COM). R represents the correlation coefficient value between each pair traces. (**d**) 3D functional connectivity map. Edges are coloured corresponding the R-value of the connection. Only strongest connections with |R|> 0.8 are kept. Nodes' s size is degree-coded. The red dot represents the COM. Scale bar: 50 μm (a).*

Results

The 3D analysis increases signal-to-noise in activity recordings. Raw 4D activity recordings displayed fluorescence contributions from active (firing) neurons, a static signal from non-active neurons and out of focus fluorescence due to the microscope's finite optical sectioning capability (Fig. 5a). As a consequence, the signal-to-noise ratio (SNR) of the raw data is SNR < 1, dominated by the background drift. Using our processing pipeline (Fig. 4) we were able to isolate active neurons from the remaining signal and thus increase the signal to noise ratio by about an order of magnitude. The background-free spatiotemporal Ca^{2+} activity AC was obtained and a movie containing only active neurons was distilled (Fig. 5a'). The denoised traces of active neurons were normalized and plotted as a function of time (Fig. 5b, for details see Materials and Methods). Comparing with manual annotation on a voxel level, we obtain a F-score of 0.18 (Materials and Methods) in the presence of strong background noise. Higher F-scores can be realized using brighter sensors such as jGCaMP8.

3D neuron cultures show patches of correlated activity. To study global connectivity of a network the time-independent pairwise correlation coefficient of two activity traces was obtained [49] (Fig. 5c) and the matrix storing the respective coefficient values was created. Differences in amplitude of two activity traces can arise from differences in activity or inhomogeneities in illumination. To obtain a correlation measure which is independent of the signal amplitudes but sensitive to common monotonic changes we used the Spearman rank correlation matrix [72]. Neuronal traces were sorted according to their distance from the center of mass (COM) of the neural culture. The correlation matrix (Fig. 5c) revealed distinguished patches of positive and negative correlation formed by neurons located both close to and far from each other. The neuronal network architecture was visualized in 3D using a graph-based representation of the connectivity matrix (Fig. 5d). Neurons were assigned as nodes connected to their neighbours by edges, colour-coded using the correlation coefficient value [73] and thresholded (|R|>0.8) [6]. The final size of the nodes was degree-coded - the more connections a neuron has the bigger the node's size (Fig. 5d). Interestingly, stronger correlations occurred between adjacent neurons as well as neurons more than 100 μm apart. Further studies using chemical or opto-genetical perturbations could reveal the interplay between far-distant neurons in the network.

Discussion

We developed a platform for fast volumetric imaging of biological samples by combining a low-complexity custom-built microscope with state-of-the-art computational tools for neuron signal extraction. The setup's complexity could be kept to a minimum by a plug and play light-sheet module that can be introduced into any standard inverted microscope, including confocal microscopes, where it replaces the condenser. As a proof of principle, we mapped the spontaneous Ca^{2+} activity in the neuronal network of a 3D neuron culture.

Spontaneous activity is a hallmark of developing neural circuits where activity patterns along with genetical programs enable their development [74-76]. In particular, synaptic refinement during neural development builds on correlation of pre- and

postsynaptic firing [77, 78]. The activity correlations we observed for small groups of neurons could initiate the emergence of a functional neuronal circuit [79]. To further investigate this, organoids at other developmental stages can be characterized using our platform. In a recent study by Sharf et al. receivers, senders and brokers nodes were identified in the human brain organoid network using multielectrode arrays [6]. Synchronous network activity at frequencies below 10 Hz (Theta-oscillations) were found. However, the classification of participating cells was challenging due to the limited access for 3D microscopy. Our light-sheet-based approach provides access both to electrophysiology at this timescale as well as neuron type through the imaging of morphological characteristics.

Finally, in order to quantify network formation and function in developing neural organoids, the spiking trains could be deduced, with the ultimate goal to develop and test *in silico* models of the biological neuronal network [68-70, 80].

Materials and Methods

Light-sheet microscope hardware. The setup features three fibre-coupled diode laser lines (488: Ibeam Smart-488-S-HP, 561: Cobolt Jive, 643: CrystaLaser LC). Light intensity was controlled with a Polychromatic Acousto-Optic Modulator (Neos, PCAOM 48062-2.5-.55). At the fibre exit, the beam gets collimated (F240FC-532, Thorlabs), split on a beam splitter (Thorlabs, BS007) (the generation of two light-sheets is possible) and is further folded by a mirror (Thorlabs, MRA05-E02) and right-angle prisms (Edmund's Optics, 84-513). Next, the beam hits a cylindrical lens (Edmund's Optics, 47763) and an aspherical lens (AMS Technologies, 354996A) which results in the formation of a static light-sheet in the field of view (FOV, 665.6 x 665.6 x 60 μm^3). Optical elements were inserted into a custom-modified Thorlabs Cage Plates (SP01).

Fluorescence detection is achieved with a water immersion objective (UMPLFLN 20XW Olympus/ 0.5, LUMPLFLN 40XW Olympus/0.8) orthogonally oriented with respect to the illumination. Collected light is detected on a camera chip (ORCA-Flash4.0 V3 Digital CMOS).

PSF determination. 3D intensity PSF was obtained by imaging 1% gel-embedded 170 nm fluorescent beads with a 561 nm laser (1% low gelling temperature agarose in ddH_2O, orange 540/560 nm beads, PS-Speck™ Microscope Point Source Kit P 7220). We cropped ten cuboids with one central bead each. For each bead we then measured 4 lateral and 2 axial intensity profiles along any two of the perpendicular axes in three central planes (*xy*, *xz*, *yz*) of the bead (Fiji) and further Gaussian-fitted them:

$$y = d + Ae^{\frac{-(x-x_0)^2}{2\sigma^2}}, \tag{1}$$

to extract $\sigma_{x,y,z}$ as a measure for the lateral and axial resolution.

To estimate the light-sheet thickness, height and homogeneity, illumination profiles across 200 x 200 μm^2 of the FOV were mapped. For this purpose, we used a $45°$ tilted mirror that was moved along the optical axis to deflect the light-sheet directly

into the detection lens. Acquired images were then 2D-gaussian fitted with a custom written Python code to extract σ_x:

$$f(x,y) = d + A\exp\left(-(\mathrm{a}(\mathrm{x}-\mathrm{x}_0)^2 + 2\mathrm{b}(\mathrm{x}-\mathrm{x}_0)(\mathrm{y}-\mathrm{y}_0) + \mathrm{c}(\mathrm{y}-\mathrm{x}_0)^2)\right) \quad (2)$$

where

$$a = \frac{cos^2\theta}{2\sigma_x^2} + \frac{sin^2\theta}{2\sigma_y^2} \quad (3)$$

$$b = \frac{-sin2\theta}{4\sigma_x^2} + \frac{sin2\theta}{4\sigma_y^2} \quad (4)$$

$$c = \frac{sin^2\theta}{2\sigma_x^2} + \frac{cos^2\theta}{2\sigma_y^2} \quad (5)$$

by setting the rotation angle to zero ($\theta = 0$) sin terms in a, b, c disappear and we get

$$f(x,y) = d + Aexp\left(-\left(\frac{(x-x_0)^2}{2\sigma_x^2} + \frac{(y-y_0)^2}{2\sigma_y^2}\right)\right). \quad (6)$$

We define the radius of the beam to be $1/e^2$ radius w_0, which will then correspond to $2\sigma_x$ and plot $2\sigma_x$ as a function of z. Data points can be fitted with the theoretical description of a Gaussian beam:

$$w(x) = w_0\sqrt{1 + \left(\frac{x-x_0}{x_R}\right)^2}, \quad (7)$$

where w_0 is the beam waist and 2 x is the Rayleigh length, x_0 corresponds to the shift with respect to the origin of the coordinate system.

Microscope control. Computer control of the setup is realized with μManager (Suppl. Fig. S1). To attain high acquisition speeds, the camera is set to streaming mode and defined at the setup's master, such that its clock drives the entire system's synchronization via TTL signals. The camera and controller of the PCAOM (Arduino 1) are loaded in the hardware configuration of μManager (https://micro-manager.org/Arduino) and can be controlled from the graphical user interface. Arduino 2 is controlled using serial commands to provide the number of steps and the direction to the controller of the piezo-positioner (SDC2). Once armed, the stage waits for triggers from Arduino 1 and moves a predefined distance after receiving a trigger. To acquire a time series, the user defines (I) the acquisition parameters in the multi-dimensional acquisition (MDA) tab of μManager (number of frames, exposure time and laser power intensity) and (II) the direction and number of z-planes via the serial command of Arduino 2. For most experiments, the exposure time is set to 10 ms per frame. Scanning was performed in a bidirectional fashion. During acquisition, the light-sheet remained at a pre-set position while the sample was moved stepwise along the

z-axis using a piezo-positioner (Smaract, SLC-1730-O20-W-L-E-NM-TI) mounted vertically. Images were saved as separate .tiff files.

Sample preparation and characterization. *Embryonic stem cell culture (ES):* Mouse embryonic stem cell line (kind gift from Yung Su Justin Kim from Dr. Ivan Bedzhov, MPI Münster) were maintained under 5% CO_2 and 37°C conditions on 10 % gelatine-coated (Sigma, G1393) T25 flasks in DMEM high glucose medium (Sigma D5671) containing 15% FBS (Sigma S0615), 100 U/ml Penicillin-Streptomycin, 2 mM L-Glutamine, 1 mM sodium pyruvate (Sigma, S8636), 0.1 mM NEAA (Sigma, M7145), 0.1 mM 2-mercaptoethanol (Sigma, M3148). Maintenance medium was freshly supplemented with 0.44 nM mLif (Amsbio, AMS-263) 0.4 μM PD 0325901 and 3 μM CHIR 99021 inhibitors (Cayman Chemicals). Seeding cell number was set to 4.2 x 10^5 cells (for 2-day interval passaging) or 1.5 x 10^5 (for 3day interval passaging). The cells carry a fluorescent marker in the nucleus (H2B–GFP+) and express a red Ca^{2+} sensor (R-GECO). The cell line was detected positive for myoplasm contamination after the experiments were performed.

Induction of neural differentiation of ES cells: The protocol to generate retina organoids was adapted from [51]. In brief, mES cells were dissociated in 0.25% EDTA trypsin (Gibco, 25200056), centrifuged (5min, 1000rpm) and resuspended in differentiation medium to achieve cell count 3 x 10^4ml. In order to form embryoid bodies, cells were allowed to reaggregate in U-bottom 96 well plates (3 x 10^3 cells per well) (Nunc). Differentiation medium was G-MEM-based (Gibco, 21710-025) supplemented with 1 mM sodium pyruvate, 0.1 mM NEAA, 0.1 M 2-mercaptoethanol and 1.5% Knockout Serum Replacement (Gibco, 10828-028). The culture was kept at 5% CO_2 and 37° C for 7 days, after which each well was filled with additional 200 ul of maturation medium I and transferred to an incubator with 40% O_2, 5% CO_2 and 37 C. Maturation medium I was DMEM/F12 supplemented with 100 U/ml Penicillin-Streptomycin and 1% N-2 Supplement (Gibco, 17502048). On day 10, spheroids were di- or tri-sectioned under a stereomicroscope (Nikon, Stereoscope), transferred to low adhesion 24-well plates (Corning, CLS3473) filled with maturation medium II and placed back into the 40% O_2, 5% CO_2, 37°C incubator. Maturation medium II was DMEM/F12 freshly supplemented with 100U Pen/Strep, 1% N_2-suplement, 0.5 μM retinoic acid (ec23®, SRP002), 1 mM taurine (Sigma, T0625). By day 15, the culture was stopped as the sample could not cultivated further, most likely due to the detected mycoplasma contamination.

Cryosectioning and immunohistochemistry: We immuno-stained 10 µm-thick sections of the sample obtained with a cryostat (Thermofisher, Cryostar nx70). After imaging, samples were fixed in 4% formaldehyde, incubated overnight in 30% sucrose and immersed in pre-warmed embedding solution (7.5% gelatin and 10% sucrose in DDI water). Blocks containing multiple organoids were cut out and frozen in -50 C isopentane bath. With confocal microscopy (LS980 Zeiss, 40x) we could detect the presence of SOX-2 (ThermoFisher, Invitrogen, eBioscience™, 14-9811-82) and Nestin (Abcam, ab81462) (Fig. 3, Suppl. Fig. S2) within the structures. For TUBB3 (Fig. 3, Suppl. Fig S2) and N-CAD (Suppl. Fig. S2) staining, samples were embedded and cryosectioned directly in Neg-50TM Frozen Section Medium (Thermo Fisher Scientific, 6502B) and stained with anti-N-Cadherin antibody (ThermoFisher, Invitrogen, PA5-

29570) and anti-Tubulin ß 3 antibody (Clone Tuj1, BioLegend, MMS-435P) respectively.

Sample mounting for imaging. The organoid was placed in an agarose well freshly prepared with the use of a 3D printed mold maker, consisting of two twin plates and a comb. First, the plates were joined together, placed on a clean surface and warm liquid 2% agarose was pipetted between them (2% high gelling temperature in ddH_2O). The comb was then placed on top of the plates and the mold maker was kept at 4° C. Once the agarose solidified, the comb was lifted and the plates were removed. As a result, we obtained a transparent block of agarose with a hollow well. We cut the well to create a single-use imaging chamber. The chamber was fixed to a bottom glass petri dish between two parafilm stripes using warm liquid agarose. Finally, the organoid was transferred to the well with a cut P200 pipette tip and the dish was filled with medium.

Imaging. We binned the camera to 4x4 to acquire 512x512 images with a frame rate of 100 fps. The volume of FOV was adjusted to 666 x 666 x 60 μm^3 with 20 z-planes and the interplane spacing set to 3 μm. We used 10 ms exposure per frame which resulted in a scanning volume rate of 5 Hz. The cells in the organoids expressed a nucleus-localized fusion protein H2B-GFP which allowed us to visualize the tissue's general architecture. We started by taking a single structural stack using 488 nm laser. Next, we performed functional imaging of the FOV (1000 time points, 200 s) using the 561 nm laser. Raw Ca^{2+} images were re-order and saved as a hyperstack using a custom-written macro (Fiji).

Image analysis. *A: Preprocessing*. The median filter applied here can be described as follows:

1. medians_over_time = Median_X(Raw_data) #spatial median for each time frame
2. Median_filtered = Raw_data – medians_over_time #for every time frame, subtract its spatial median

The Fourier filter described above is performed before motion-correction and after bleach-correction. Mathematically, it consists of the following steps:

1. f = FFT_X(Median_filtered) #scipy.fft.rfftn module in python
2. var = VAR_T(f)
3. binmask = LOG_10(var) < thr (=10.5)
4. transform_back = binmask * f (multiply each volume at every time point)
5. Variance_filtered = IFFT_X(transform_back) #scipy.fft.irfftn in python

B: Trace extraction with Caiman. To extract spatial footprints of active neurons and their corresponding Ca^{2+} traces we used the Caiman 1.9.9 package. CNMF algorithm was run twice on motion corrected and memory mapped data. For motion correction, relevant parameters were set to

- strides = (18, 18, 4), overlaps = (9, 9, 2), max_shifts = (4, 4, 2), max_deviation_rigid = 5.

For the CNMF fit

- rf = 10, stride = 10, K = 10, gSig = [2,2,2], merge_thresh = 0.8, nb = 2, p = 2.

were selected. After the first fit, identified components were evaluated and only those displaying a peak SNR ≥ 1 and a spatial correlation ≥ 0.5 were accepted. The CNMF was then run again on the whole FOV seeded with the accepted components. Output components were then manually curated to filter-out the spurious ones. Each denoised trace was individually normalized $\Delta F/F = (F - F_{min})/(F_{max} - F_{min})$, where F_{max} and F_{min} were the highest and lowest intensities recorded in the trace, respectively. Spearman rank correlation matrix was constructed using fluorescent traces of active neurons, ordered according to their distance from the organoid's centre of mass using the seaborn package (0.11.2). Using the spatial coordinates of identified components in the FOV, we could reconstruct the network as a graph, where nodes represent neurons and edges the interactions between them. The edges adapt the colours corresponding the R-value of the connection as calculated previously in the matrix. To display only the strongest interactions, a threshold was set on edges to show connections with |R|> 0.8. The node size is then degree-coded so potential hubs in the network can be identified.

C. Postprocessing: We chose as spatial thresholds a minimum neuron volume of min_vol ($710\ \mu m^3$) and a maximum neuron volume of max_vol ($7605\ \mu m^3$) volume, estimated from manual annotations of the raw data. The variance threshold was chosen empirically after looking at the original output of the CaImAn software, and was chosen to be var_thr_post (0.6).

CaImAn segmentation performance: To estimate the performance of our software pipeline we annotated 3 crops from 3 slices in the dataset from figure 4 (z-slice=6,12,18) by hand. Two annotators independently annotated the slices, and then the intersection of the annotations was taken to be a “consensus annotation”, for each crop respectively (but all z-slices combined). We overlaid the consensus annotation to the spatial segmentation of the CaImAn software and calculate precision, recall and F1-score metrics (https://en.wikipedia.org/wiki/F-score). We obtain a precision of 13%, a recall of 32% and an F1-score of 18% when comparing the consensus annotation with the CaImAn result. This evaluates the spatial segmentation performance on a single voxel level, which is a rather strict quality criterion. Also, since the annotations are performed on the raw data, which is not motion corrected yet, motion artifacts systematically lower the performance metrics.

Acknowledgments. We thank Otger Campas and Paul Hansma for initial discussions, Carolyne Sheline and Nicoleta Dahnovici for contributions in the early phases of the project, Jacopo Di Russo and Jennifer Diemer for help with the stem cell culture and Joachim Spatz for his generous support. In addition, we thank Johannes Friedrich and Andrea Giovannuci for stimulating discussions.

Disclosures. The authors declare no conflicts of interest.

Data availability. Data underlying the results presented in this paper are not publicly available at this time but may be obtained from the authors upon request.

Funding information. This project has received funding from the European Research Council (ERC) under the European Union’s Horizon 2020 research and innovation program (Grant Agreement No. 850691), the Center for NanoScience (CeNS) at the

Ludwig-Maximilian-University (LMU) Munich, and the Munich Cluster for Systems Neurology (SyNergy).

Bibliography

1. A. Giovannucci, J. Friedrich, P. Gunn, J. Kalfon, B. L. Brown, S. A. Koay, J. Taxidis, F. Najafi, J. L. Gauthier, P. Zhou, B. S. Khakh, D. W. Tank, D. B. Chklovskii, and E. A. Pnevmatikakis, "CaImAn an open source tool for scalable calcium imaging data analysis," eLife **8**, e38173 (2019).
2. M. A. Lancaster, M. Renner, C.-A. Martin, D. Wenzel, L. S. Bicknell, M. E. Hurles, T. Homfray, J. M. Penninger, A. P. Jackson, and J. A. Knoblich, "Cerebral organoids model human brain development and microcephaly," Nature **501**, 373–379 (2013).
3. A. P. Passaro, and S. L. Stice, "Electrophysiological analysis of brain organoids current approaches and advancements," Frontiers in Neuroscience **14**, 622137 (2021).
4. M. O'Hara-Wright, and A. Gonzalez-Cordero, "Retinal organoids: a window into human retinal development," Development **147**, dev189746 (2020).
5. S. L. Giandomenico, S. B. Mierau, G. M. Gibbons, L. M. D. Wenger, L. Masullo, T. Sit, M. Sutcliffe, J. Boulanger, M. Tripodi, E. Derivery, O. Paulsen, A. Lakatos, and M. A. Lancaster, "Cerebral organoids at the air–liquid interface generate diverse nerve tracts with functional output," Nature Neuroscience **22**, 669–679 (2019).
6. T. Sharf, T. Molen, E. Guzman, S. M. K. Glasauer, G. Luna, Z. Cheng, M. Audouard, K. G. Ranasinghe, K. Kudo, S. S. Nagarajan, K. R. Tovar, L. R. Petzold, P. K. Hansma, and K. S. Kosik, "Intrinsic network activity in human brain organoids," BioRxiv (2021).
7. A. Minovi, A. Aguado, D. Brunert, S. Kurtenbach, S. Dazert, H. Hatt, and H. Conrad, "Isolation, culture optimization and functional characterization of stem cell neurospheres from mouse neonatal olfactory bulb and epithelium," Eur Arch Otorhinolaryngol **274**, 3071-3085 (2017).
8. P. Gervois, T. Struys, P. Hilkens, A. Bronckaers, J. Ratajczak, C. Politis, B. Brone, I. Lambrichts, and W. Martens, "Neurogenic maturation of human dental pulp stem cells following neurosphere generation induces morphological and electrophysiological characteristics of functional neurons," Stem Cells Dev **24**, 296-311 (2015).
9. A. M. Paşca, S. A. Sloan, L. E. Clarke, Y. Tian, C. D. Makinson, N. Huber, C. H. Kim, J.-Y. Park, N. A. O'Rourke, K. D. Nguyen, S. J. Smith, J. R. Huguenard, D. H. Geschwind, B. A. Barres, and S. P. Paşca, "Functional cortical neurons and astrocytes from human pluripotent stem cells in 3D culture," Nature Methods **12**, 671–678 (2015).
10. R. Li, L. Sun, A. Fang, P. Li, Q. Wu, and X. Wang, "Recapitulating cortical development with organoid culture in vitro and modeling abnormal spindle-like (ASPM related primary) microcephaly disease," Protein & Cell **8**, 823-833 (2017).
11. E. Di Lullo, and A. R. Kriegstein, "The use of brain organoids to investigate neural development and disease," Nature Reviews Neuroscience **18**, 573–584 (2017).
12. B. Cakir, Y. Xiang, Y. Tanaka, M. H. Kural, M. Parent, Y.-J. Kang, K. Chapeton, B. Patterson, Y. Yuan, C.-S. He, M. S. B. Raredon, J. Dengelegi, K.-Y. Kim, P. Sun, M. Zhong, S. Lee, P. Patra, F. Hyder, L. E. Niklason, S.-H. Lee, Y. Young, and I.-H. Park, "Engineering of human brain organoids with a functional vascular-like system," Nature Methods **16**, 1169–1175 (2019).
13. X. Zhong, C. Gutierrez, T. Xue, C. Hampton, M. N. Vergara, L. H. Cao, A. Peters, T. S. Park, E. T. Zambidis, J. S. Meyer, D. M. Gamm, K.-W. Yau, and M. V. Canto-Soler, "Generation of three-dimensional retinal tissue with functional photoreceptors from human iPSCs," Nature Communications **5**, 1-14 (2014).
14. J. Li, Y. Chen, S. Ouyang, J. Ma, H. Sun, L. Luo, S. Chen, and Y. Liu, "Generation and Staging of Human Retinal Organoids Based on Self-Formed Ectodermal Autonomous Multi-Zone System," Front Cell Dev Biol **9**, 732382 (2021).
15. S. Kim, A. Lowe, R. Dharmat, S. Lee, L. A. Owen, J. Wang, A. Shakoor, Y. Li, D. J. Morgan, A. A. Hejazi, A. Cvekl, M. M. DeAngelis, Z. J. Zhou, R. Chen, and W. Liu, "Generation, transcriptome profiling, and functional validation of cone-rich human retinal organoids," Proceedings of the National Academy of Sciences of the United States of America **116**, 10824-10833 (2019).
16. M. Mayer, O. Arrizabalaga, F. Lieb, M. Ciba, S. Ritter, and C. Thielemann, "Electrophysiological investigation of human embryonic stem cell derived neurospheres using a novel spike detection algorithm," Biosensors and Bioelectronics **100**, 462-468 (2018).
17. C. A. Trujillo, R. Gao, P. D. Negraes, J. Gu, J. Buchanan, S. Preissl, A. Wang, W. Wu, G. G. Haddad, I. A. Chaim, A. Domissy, M. Vandenberghe, A. Devor, G. W. Yeo, B. Voytek, and A. R. Muotri, "Complex Oscillatory Waves Emerging from Cortical Organoids Model Early Human Brain Network Development," Cell Stem Cell **25**, 558-569 (2019).
18. T. J. Shafer, J. P. Brown, B. Lynch, S. Davila-Montero, K. Wallace, and K. P. Friedman, "Evaluation of Chemical Effects on Network Formation in Cortical Neurons Grown on Microelectrode Arrays," Toxicological Sciences **169**, 436-455 (2019).
19. G. Quadrato, T. V. Nguyen, E. Z. Macosko, J. L. Sherwood, S. M. Yang, D. R. Berger, N. Maria, J. Scholvin, M. Goldman, J. P. Kinney, E. S. Boyden, J. W. Lichtman, Z. Williams, S. A. McCarroll, and P. Arlotta, "Cell diversity and network dynamics in photosensitive human brain organoids," Nature **545**, 48–53 (2017).

20. E. R. McConnell, M. A. McClain, J. Ross, W. R. LeFew, and T. J. Shafer, "Evaluation of multi-well microelectrode arrays for neurotoxicity screening using a chemical training set," Neurotoxicology **33**, 1048-1057 (2017).
21. D. Hallam, G. Hilgen, B. Dorgau, L. Zhu, M. Yu, S. Bojic, P. Hewitt, M. Schmitt, M. Uteng, S. Kustermann, D. H. W. Steel, M. Nicholds, R. J. Thomas, A. Treumann, A. Porter, E. Sernagor, L. Armstrong, and M. Lako, "Human Induced Pluripotent Stem Cells Generate Light Responsive Retinal Organoids with Variable and Nutrient Dependent Efficiency," Stem Cells **36**, 1535-1551 (2018).
22. C. L. Frank, J. P. Brown, K. Wallace, W. R. Mundy, and T. J. Shafer, "From the Cover: Developmental Neurotoxicants Disrupt Activity in Cortical Networks on Microelectrode Arrays: Results of Screening 86 Compounds During Neural Network Formation," Toxicological Sciences **160**, 121-135 (2017).
23. M. Durens, J. E. Nestor, M. Williams, K. Herold, R. F. Niescier, J. W. Lunden, A. W. Phillips, Y.-C. Lin, D. M. Dykxhoorn, and M. W. Nestor, "High-throughput screening of human induced pluripotent stem cell-derived brain organoids," Journal of Neuroscience Methods **335**, 108627 (2020).
24. E. Cotterill, D. Hall, K. Wallace, W. R. Mundy, S. J. Eglen, and T. J. Shafer, "Characterization of Early Cortical Neural Network Development in Multiwell Microelectrode Array Plates," Journal of Biomolecular Screening **21**, 510-519 (2016).
25. T. Gollisch, and M. Meister, "Eye smarter than scientists believed: Neural computations in circuits of the retina," Neuron **65**, 150-164 (2010).
26. M. Fathi, C. T. Ross, and Z. Hosseinzadeh, "Functional 3-Dimensional Retinal Organoids: Technological Progress and Existing Challenges," Frontiers in Neuroscience **15**, 668857 (2021).
27. C. Grienberger, and A. Konnerth, "Imaging Calcium in Neurons," Neuron **73**, 862-885 (2012).
28. R. A. Samarasinghe, O. A. Miranda, J. E. Buth, S. Mitchell, I. Ferando, M. Watanabe, T. F. Allison, A. Kurdian, N. N. Fotion, M. J. Gandal, P. Golshani, K. Plath, W. E. Lowry, J. M. Parent, I. Mody, and B. G. Novitch, "Identification of neural oscillations and epileptiform changes in human brain organoids," Nat Neurosci **24**, 1488-1500 (2021).
29. H. Sakaguchi, Y. Ozaki, T. Ashida, T. Matsubara, N. Oishi, S. Kihara, and J. Takahashi, "Self-Organized Synchronous Calcium Transients in a Cultured Human Neural Network Derived from Cerebral Organoids," Stem Cell Reports **13**, 458-473 (2019).
30. C. S. Cowan, M. Renner, M. De Gennaro, B. Gross-Scherf, D. Goldblum, Y. Hou, M. Munz, T. M. Rodrigues, J. Krol, T. Szikra, R. Cuttat, A. Waldt, P. Papasaikas, R. Diggelmann, C. P. Patino-Alvarez, P. Galliker, S. E. Spirig, D. Pavlinic, N. Gerber-Hollbach, S. Schuierer, A. Srdanovic, M. Balogh, R. Panero, A. Kusnyerik, A. Szabo, M. B. Stadler, S. Orgül, S. Picelli, P. W. Hasler, A. Hierlemann, H. P. N. Scholl, G. Roma, F. Nigsch, and B. Roska, "Cell Types of the Human Retina and Its Organoids at Single-Cell Resolution," Cell **182**, 1623-1640 (2020).
31. W. Zong, H. A. Obenhaus, E. R. Skytøen, H. Eneqvist, N. L. Jong, M. R. Jorge, M.-B. Moser, and E. I. Moser, "Large-scale two-photon calcium imaging in freely moving mice," Cell **185**, 1240-1256 (2021).
32. S. Weisenburger, F. Tejera, J. Demas, B. Chen, J. Manley, F. T. Sparks, F. M. Traub, T. L. Daigle, H. Zeng, A. Losonczy, and A. Vaziri, "Volumetric Ca2+ Imaging in the Mouse Brain Using Hybrid Multiplexed Sculpted Light Microscopy," Cell **177**, 1050-1066 (2019).
33. S. Quirin, N. Vladimirov, C. T. Yang, D. S. Peterka, R. Yuste, and M. B. Ahrens, "Calcium imaging of neural circuits with extended depth-of-field light-sheet microscopy," Opt Lett **41**, 855-858 (2016).
34. R. Prevedel, A. J. Verhoef, A. J. Pernía-Andrade, S. Weisenburger, B. S. Huang, T. Nöbauer, A. Fernández, J. E. Delcour, P. Golshani, A. Baltuška, and A. Vaziri, "Fast volumetric calcium imaging across multiple cortical layers using sculpted light," Nature Methods **13**, 1021–1028 (2016).
35. T. Panier, S. A. Romano, R. Olive, T. Pietri, G. Sumbre, R. Candelier, and G. Debrégeas, "Fast functional imaging of multiple brain regions in intact zebrafish larvae using Selective Plane Illumination Microscopy," Frontiers in Neural Circuits **7**, 65 (2013).
36. D. A. Markov, L. Petrucco, A. M. Kist, and R. Portugues, "A cerebellar internal model calibrates a feedback controller involved in sensorimotor control," Nature Communications **12**, 1-21 (2021).
37. S. Han, W. Yang, and R. Yuste, "Two-Color Volumetric Imaging of Neuronal Activity of Cortical Columns," Cell Reports **27**, 2229-2240 (2019).
38. M. dal Maschio, J. C. Donovan, T. O. Helmbrecht, and H. Baier, "Linking Neurons to Network Function and Behavior by Two-Photon Holographic Optogenetics and Volumetric Imaging," Neuron **94**, 774-789 (2017).
39. N. Wagner, F. Beuttenmueller, N. Norlin, J. Gierten, J. C. Boffi, J. Wittbrodt, M. Weigert, L. Hufnagel, R. Prevedel, and A. Kreshuk, "Deep learning-enhanced light-field imaging with continuous validation," Nature Methods **18**, 557–563 (2021).
40. Z. Zhang, L. Bai, L. Cong, P. Yu, T. Zhang, W. Shi, F. Li, J. Du, and K. Wang, "Imaging volumetric dynamics at high speed in mouse and zebrafish brain with confocal light field microscopy," Nature Biotechnology **39**, 74–83 (2020).
41. V. Voleti, K. Patel, W. Li, C. P. Campos, S. Bharadwaj, H. Yu, C. Ford, M. J. Casper, R. W. Yan, W. Liang, C. Wen, K. D. Kimura, K. L. Targoff, and E. M. C. Hillman, "Real-time volumetric microscopy of in vivo dynamics and large-scale samples with SCAPE 2.0," Nature Methods **16**, 1054-1062 (2019).
42. N. Vladimirov, Y. Mu, T. Kawashima, D. V. Bennett, C.-T. Yang, L. L. Looger, P. J. Keller, J. Freeman, and M. B. Ahrens, "Light-sheet functional imaging in fictively behaving zebrafish," Nature Methods **11**, 883–884 (2014).

43. R. Prevedel, Y.-G. Yoon, M. Hoffmann, N. Pak, G. Wetzstein, S. Kato, T. Schrödel, R. Raskar, M. Zimmer, E. S. Boyden, and A. Vaziri, "Simultaneous whole-animal 3D imaging of neuronal activity using light- field microscopy," Nature Methods **11**, 727–730 (2014).
44. W. C. Lemon, S. R. Pulver, B. Höckendorf, K. McDole, K. Branson, J. Freeman, and P. J. Keller, "Whole-central nervous system functional imaging in larval Drosophila," Nature Communications **6**, 1-16 (2015).
45. L. Kong, J. Tang, J. P. Little, Y. Yu, T. Lammermann, C. P. Lin, R. N. Germain, and M. Cui, "Continuous volumetric imaging via an optical phase-locked ultrasound lens," Nat Methods **12**, 759-762 (2015).
46. C. J. Greer, and T. E. Holy, "Fast objective coupled planar illumination microscopy," Nature Communications **10** (2019).
47. J. Demas, J. Manley, F. Tejera, K. Barber, H. Kim, F. M. Traub, B. Chen, and A. Vaziri, "High-speed, cortex-wide volumetric recording of neuroactivity at cellular resolution using light beads microscopy," Nature Methods **18**, 1103-1111 (2021).
48. M. B. Bouchard, V. Voleti, C. S. Mendes, C. O. Lacefield, W. B. Grueber, R. S. Mann, R. M. Bruno, and E. M. C. Hillman, "Swept confocally-aligned planar excitation (SCAPE) microscopy for high speed volumetric imaging of behaving organisms," Nature Photonics **9**, 113-119 (2015).
49. M. B. Ahrens, M. B. Orger, D. N. Robson, J. M. Li, and P. J. Keller, "Whole-brain functional imaging at cellular resolution using light-sheet microscopy," Nature Methods **10**, 413–420 (2013).
50. V. Pérez Koldenkova, and T. Nagai, "Genetically encoded Ca2+ indicators: Properties and evaluation," Biochimica et Biophysica Acta (BBA) - Molecular Cell Research **1833**, 1787-1797 (2013).
51. M. Völkner, M. Zschatzsch, M. Rostovskaya, R. W. Overall, V. Busskamp, K. Anastassiadis, and M. O. Karl, "Retinal Organoids from Pluripotent Stem Cells Efficiently Recapitulate Retinogenesis," Stem Cell Reports **6**, 525-538 (2016).
52. M. V. Zappone, R. Galli, R. Catena, N. Meani, S. D. Biasi, E. Mattei, C. Tiveron, A. L. Vescovi, R. Lovell-Badge, S. Ottolenghi, and S. K. Nicolis, "Sox2 regulatory sequences direct expression of a (beta)-geo transgene to telencephalic neural stem cells and precursors of the mouse embryo, revealing regionalization of gene expression in CNS stem cells," Development **127**, 2367-2382 (2000).
53. U. Lendahl, L. B. Zimmerman, and R. D. G. McKay, "CNS stem cells express a new class of intermediate filament protein," Cell **60**, 585-595 (1990).
54. P. Ellis, B. M. Fagan, S. T. Magness, S. R. Hutton, O. Taranova, S. Hayashi, A. P. McMahon, M. S. Rao, and L. H. Pevny, "SOX2, a Persistent Marker for Multipotential Neural Stem Cells Derived from Embryonic Stem Cells, the Embryo or the Adult," Developmental Neuroscience **26**, 148-165 (2004).
55. J. Dahlstrand, M. Lardelli, and U. Lendahl, "Nestin mRNA expression correlates with the central nervous system progenitor cell state in many, but not all, regions of developing central nervous system," Developmental Brain Research **84**, 109-129 (1995).
56. M. Winiecka-Klimek, M. Smolarz, M. P. Walczak, J. Zieba, K. Hulas-Bigoszewska, B. Kmieciak, S. Piaskowski, P. Rieske, D. P. Grzela, and E. Stoczynska-Fidelus, "SOX2 and SOX2-MYC Reprogramming Process of Fibroblasts to the Neural Stem Cells Compromised by Senescence," PLOS ONE **10**, e0141688 (2015).
57. A. L. Jiménez-Vaca, G. Benitez-King, V. Ruiz, G. B. Ramírez-Rodríguez, B. Hernández-De La Cruz, F. A. Salamanca-Gómez, H. González-Márquez, I. Ramírez-Sánchez, L. Ortíz-López, C. Vélez-Del Valle, and R. M. Ordoñez-Razo, "Exfoliated Human Olfactory Neuroepithelium: A Source of Neural Progenitor Cells," Molecular Neurobiology **55**, 2516-2523 (2018).
58. L. S. Wright, I. Pinilla, J. Saha, J. M. Clermont, J. S. Lien, K. D. Borys, E. E. Capowski, M. J. Phillips, and D. M. Gamm, "VSX2 and ASCL1 Are Indicators of Neurogenic Competence in Human Retinal Progenitor Cultures," PLOS ONE **10**, e0135830 (2015).
59. S.-T. Lee, K. Chu, K.-H. Jung, Y.-M. Song, D. Jeon, S. U. Kim, M. Kim, S. K. Lee, and J.-K. Roh, "Direct Generation of Neurosphere-Like Cells from Human Dermal Fibroblasts," PLoS ONE **6**, e21801 (2011).
60. J. Akerboom, N. Carreras Calderón, L. Tian, S. Wabnig, M. Prigge, J. Tolö, A. Gordus, M. Orger, K. Severi, J. Macklin, R. Patel, S. Pulver, T. Wardill, E. Fischer, C. Schüler, T.-W. Chen, K. Sarkisyan, J. Marvin, C. Bargmann, D. Kim, S. Kügler, L. Lagnado, P. Hegemann, A. Gottschalk, E. Schreiter, and L. Looger, "Genetically encoded calcium indicators for multi-color neural activity imaging and combination with optogenetics," Frontiers in Molecular Neuroscience **6** (2013).
61. P. Kaifosh, J. D. Zaremba, N. B. Danielson, and A. Losonczy, "SIMA: Python software for analysis of dynamic fluorescence imaging data," Front Neuroinform **8**, 80 (2014).
62. P. Zhou, S. L. Resendez, J. Rodriguez-Romaguera, J. C. Jimenez, S. Q. Neufeld, A. Giovannucci, J. Friedrich, E. A. Pnevmatikakis, G. D. Stuber, R. Hen, M. A. Kheirbek, B. L. Sabatini, R. E. Kass, and L. Paninski, "Efficient and accurate extraction of in vivo calcium signals from microendoscopic video data," eLife **7** (2018).
63. M. Pachitariu, C. Stringer, M. Dipoppa, S. Schröder, L. F. Rossi, H. Dalgleish, M. Carandini, and K. D. Harris, "Suite2p: beyond 10,000 neurons with standard two-photon microscopy," Biorivix (2017).
64. S. Reynolds, T. Abrahamsson, R. Schuck, P. J. Sjostrom, S. R. Schultz, and P. L. Dragotti, "ABLE: An Activity-Based Level Set Segmentation Algorithm for Two-Photon Calcium Imaging Data," eNeuro **4** (2017).
65. A. Petersen, N. Simon, and D. Witten, "Scalpel: Extracting Neurons from Calcium Imaging Data," Ann Appl Stat **12**, 2430-2456 (2018).
66. J. Lu, C. Li, J. Singh-Alvarado, Z. C. Zhou, F. Frohlich, R. Mooney, and F. Wang, "MIN1PIPE: A Miniscope 1-Photon-Based Calcium Imaging Signal Extraction Pipeline," Cell Rep **23**, 3673-3684 (2018).

67. M. Rueckl, S. C. Lenzi, L. Moreno-Velasquez, D. Parthier, D. Schmitz, S. Ruediger, and F. W. Johenning, "SamuROI, a Python-Based Software Tool for Visualization and Analysis of Dynamic Time Series Imaging at Multiple Spatial Scales," Front Neuroinform **11**, 44 (2017).
68. E. A. Pnevmatikakis, D. Soudry, Y. Gao, T. A. Machado, J. Merel, D. Pfau, T. Reardon, Y. Mu, C. Lacefield, W. Yang, M. Ahrens, R. Bruno, T. M. Jessell, D. S. Peterka, R. Yuste, and L. Paninski, "Simultaneous Denoising, Deconvolution, and Demixing of Calcium Imaging Data," Neuron **89**, 285-299 (2016).
69. J. T. Vogelstein, A. M. Packer, T. A. Machado, T. Sippy, B. Babadi, R. Yuste, and L. Paninski, "Fast nonnegative deconvolution for spike train inference from population calcium imaging," J Neurophysiol **104**, 3691-3704 (2010).
70. J. Friedrich, P. Zhou, and L. Paninski, "Fast online deconvolution of calcium imaging data," PLoS Comput Biol **13**, e1005423 (2017).
71. E. H. K. Stelzer, F. Strobl, B.-J. Chang, F. Preusser, S. Preibisch, K. McDole, and R. Fiolka, "Light sheet fluorescence microscopy," Nature Reviews Methods Primers **1**, 1-25 (2021).
72. G. Rousselet, and C. Pernet, "Improving standards in brain-behavior correlation analyses," Frontiers in Human Neuroscience **6**, 119 (2012).
73. M. Koutrouli, E. Karatzas, D. Paez-Espino, and G. A. Pavlopoulos, "A Guide to Conquer the Biological Network Era Using Graph Theory," Frontiers in Bioengineering and Biotechnology **8** (2020).
74. R. Khazipov, and H. J. Luhmann, "Early patterns of electrical activity in the developing cerebral cortex of humans and rodents," Trends in Neurosciences **29**, 414-418 (2006).
75. A. G. Blankenship, and M. B. Feller, "Mechanisms underlying spontaneous patterned activity in developing neu ral circuits," Nature Reviews Neuroscience **11** (2010).
76. Y. Ben-Ari, "Developing networks play a similar melody," Trends Neurosci **24**, 353-360 (2001).
77. D. Hebb, "The organization of behavior: a neuropsychological theory," New York: Wiley (1949).
78. G. Bi, and M. Poo, "Synaptic modification by correlated activity: Hebb's postulate revisited," Annu Rev Neurosci **24**, 139-166 (2001).
79. M. Meister, R. O. L. Wong, D. A. Baylor, and C. J. Shatz, "Synchronous Bursts of Action Potentials in Ganglion Cells of the Developing Mammalian Retina," Science **252**, 939-943 (1991).
80. T. Deneux, A. Kaszas, G. Szalay, G. Katona, T. Lakner, A. Grinvald, B. Rozsa, and I. Vanzetta, "Accurate spike estimation from noisy calcium signals for ultrafast three-dimensional imaging of large neuronal populations in vivo," Nat Commun **7**, 12190 (2016).
81. R. Lu, W. Sun, Y. Liang, A. M. Kerlin, J. Bierfeld, J. D. Seelig, D. E. Wilson, B. Scholl, B. Mohar, M. Tanimoto, M. Koyama, D. Fitzpatrick, M. B. Orger, and N. Ji, "Video-rate volumetric functional imaging of the brain at synaptic resolution," Nature Neuroscience **20**, 620-628 (2017).
82. R. Lu, M. Tanimoto, M. Koyama, and N. Ji, "50 Hz volumetric functional imaging with continuously adjustable depth of focus," Biomedical Optics Express **9**, 1964-1976 (2018).
83. S. Xiao, H.-A. Tseng, H. Gritton, X. Han, and J. Mertz, "Video-rate volumetric neuronal imaging using 3D targeted illumination," Scientific Reports **8**, 1-10 (2018).
84. B. Yang, M. Lange, A. Millett-Sikking, X. Zhao, J. Bragantini, S. Vijaykumar, M. Kamb, R. Gómez-Sjöberg, A. C. Solak, W. Wang, H. Kobayashi, M. N. McCarroll, L. W. Whitehead, R. P. Fiolka, T. B. Kornberg, A. G. York, and L. A. Royer, "DaXi—high-resolution, large imaging volume and multi-view single-objective light-sheet microscopy," Nature Methods **19**, 461-469 (2022).
85. K. A. Venstrom, and L. F. Reichardt, "Extracellular Matrix 2: Role of extracellular matrix molecules and their receptors in the nervous system," The FASEB Journal **7**, 996-1003 (1993).
86. P. Goichberg, and B. Geiger, "Direct Involvement of N-Cadherin–mediated Signaling in Muscle Differentiation," Molecular Biology of the Cell **9**, 3119-3131 (1998).
87. M. George-Weinstein, J. Gerhart, J. Blitz, E. Simak, and K. K. A., "N-cadherin Promotes the Commitment and Differentiation of Skeletal Muscle Precursor Cells," Developmental Biology **185**, 14-24 (1997).
88. J. L. Bixby, G. B. Grunwald, and R. J. Bookman, "Ca2+ influx and neurite growth in response to purified N-cadherin and laminin," Journal of Cell Biology **127**, 1461-1475 (1994).